Irregular dynamics of cellular blood flow in a model microvessel

Spencer H. Bryngelson,[1,*] Florimond Guéniat,[2] and Jonathan B. Freund[1,3]

[1]*Department of Mechanical Science & Engineering, University of Illinois at Urbana–Champaign, Urbana, Illinois 61801, USA*

[2]*The Center for Exascale Simulation of Plasma-coupled Combustion, University of Illinois at Urbana–Champaign, Urbana, Illinois 61801, USA*

[3]*Department of Aerospace Engineering University of Illinois at Urbana–Champaign, Urbana, Illinois 61801, USA*

(Received 21 March 2019; published 8 July 2019)

The flow of red blood cells within cylindrical vessels is complex and irregular, so long as the vessel diameter is somewhat larger than the nominal cell size. Long-time-series simulations, in which cells flow 10^5 vessel diameters, are used to characterize the chaotic kinematics, particularly to inform reduced-order models. The simulation model used includes full coupling between the elastic red blood cell membranes and surrounding viscous fluid, providing a faithful representation of the cell-scale dynamics. Results show that the flow has neither classifiable recurrent features nor a dominant frequency. Instead, its kinematics are sensitive to the initial flow configuration in a way consistent with chaos and Lagrangian turbulence. Phase-space reconstructions show that a low-dimensional attractor does not exist, so the observed long-time dynamics are effectively stochastic. Based on this, a simple Markov chain model for the dynamics is introduced and shown to reproduce the statistics of the cell positions.

DOI: 10.1103/PhysRevE.100.012203

I. INTRODUCTION

Blood is a complex suspension whose primary components are red blood cells suspended in plasma. Red cells typically make up between 20% and 45% of whole blood by volume, depending upon the vessel size [1,2]. The next most substantial contributions are from white blood cells and platelets, though together they contribute less than 2% to the volume of whole blood [3], and thus the cell-scale dynamics are generally dominated by red blood cells [4], which are flexible elastic membranes encasing a hemoglobin solution called the cytosol. The motion of red cells typically appears disordered, as shown in Fig. 1, except when the confining vessel diameter is smaller than the nominal cell diameter [7–10], for which the cells flow in linearly stable trains [11,12]. Though blood was one of the first complex fluids to be studied [13,14], its irregular flow behaviors remain crudely described and challenging to predict.

The kinematics of the cellular flow are important for many biomedical applications: the design of microfluidic devices that operate on flowing cells [15,16], targeted drug delivery [17–19] and screening [20,21], and the development of artificial blood [22,23] and organs [24–26], among others. Fully describing these flows is challenging. The small spatiotemporal scales often hinder accurate experimental observations [27], and while computer simulations are not limited in this regard, even basic flow predictions require sophisticated numerical techniques and significant computational resources [28]. Thus, reduced-order models are potentially useful for guiding engineering design. Continuum models based upon rheological fluids are successful examples of this, but they are best suited to reproduce the mean-flow properties of blood when the confining geometry is significantly larger than the individual cells [29–32]. We aim to characterize the irregular single-cell-scale motion to facilitate the development of reduced-order models that represent their behavior.

The dynamics of irregular flows can be classified as chaotic or nonchaotic. Chaotic dynamics are well understood to have a fractal character and exhibit extreme sensitivity to initial conditions. Even seemingly simple and dissipative Stokes flows can exhibit this property: perturbations to three rigid spheres suspended in a rotating cylinder [33], sedimenting under gravity [34], or in confined shear flow [35] diverge exponentially, a property often called chaotic advection [36,37] or Lagrangian turbulence [38,39]. However, not all irregular flows are chaotic; a flow system need not be extremely sensitive to the initial conditions to be mechanically unstable in a way consistent with the kinematics observed of red blood cells in the microcirculation. Further, the highly dissipative mechanics of the confined low Reynolds number (<0.01; see Sec. III) flow might indicate a suppression of chaotic kinematics.

We consider whether or not this flow has an associated strange attractor that can characterize the dynamics with fewer degrees of freedom than the full system. However, this is not obvious from simple direct observations: low- and high-dimensional chaotic behavior can appear qualitatively similar, as shown in Fig. 2. After we assess its existence in Sec. IV B, we consider its dimension D. The extensively studied Lorenz system has a relatively low-dimensional attractor, $D = 2.06$ [43], which allows for a reduced description of the dynamics [44]. Turbulent fluid flow also has a strange attractor [45–47], though for streamwise periodic channel flow its dimension is large $D \gg 1$ (Keefe *et al.* [48] estimated $D > 780$, though faithful estimation of such large dimensionality is challenging

*spencer@caltech.edu; sbryngelson@gmail.com

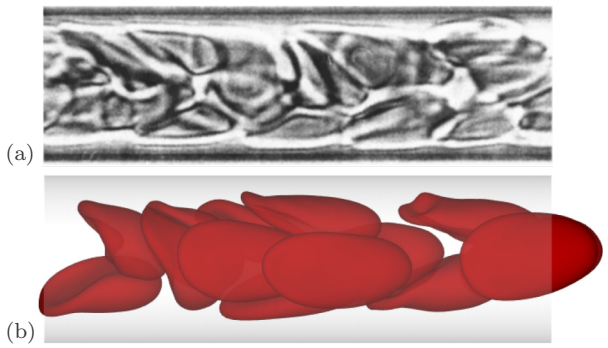

FIG. 1. Cellular blood flow in a tube as (a) observed *in vitro* [5] and (b) simulated using numerical techniques. Figure reprinted with permission from Microcirculation in Ref. [6].

[49]). This is important for model reduction, since such high dimensionality means that the dynamics cannot be reduced to a few degrees of freedom. This precludes common methods for describing the dynamics, such as Poincaré sections and return maps, and prohibits attractor reconstruction [50].

In crafting a reduced statistical model, it is also important to consider the possibility of stochastic behaviors. Stochastic systems are probabilistic and random, and thus have no underlying strange attractor. As a result, different methods are needed to model the statistics. This is true even though such systems show qualitative similarities to chaotic systems, such as the heart-rate signal of Fig. 2(c). Observables of high-dimensional chaotic systems, such as isotropic turbulence [51], solar winds [52], electrical discharge fluctuation [53], and gel transitions [54], can be quantitatively indistinguishable from those of a stochastic system. Thus, given the difficulty of reconstructing the high-dimensional attractor, such systems have sometimes been modeled as stochastic processes. To this end, Markov, Langevin, and Lévy processes have been able to reproduce the statistics of the true nonlinear chaotic dynamics [55,56], whereas otherwise attractive linear models (e.g., autoregressive moving average models) have not [57].

Our physically faithful computational model for the flowing red blood cells consists of a three-dimensional Stokes flow of elastic capsules confined in a rigid tube model of a microvessel, such as is typical in the microcirculation or microfluidic devices. The simulation model and specific flow configuration are described in Sec. II, along with a discussion of its physical validity as a mathematical model for actual flowing blood cells. The numerical methods used to solve for the flow, which include full coupling between the viscous fluid and elastic cell membranes, are summarized in Sec. III.

Our statistical modeling goal is linked to the characteristics of the basic kinematic behavior of flowing red blood cells. Assessing this involves analyzing the chaotic and stochastic characteristics of the flow observables. In Sec. IV A, we introduce the long-time flow used for this analysis. Space–time correlations and Fourier power spectra are used to probe for any recurrent behaviors and frequencies. Chaotic dynamics are addressed in Sec. IV B, wherein we assess their existence, bound their dimensionality, and make quantitative comparisons with stochastic behaviors. In Sec. IV C, we use these results to guide the development of a reduced-order statistical model for the flow. A summary and discussion of our results are presented in Sec. V.

II. MODEL FLOW AND KINEMATIC METRICS

A schematic of the model flow system is shown in Fig. 3. The streamwise-periodic cylindrical model microvessel has diameter $D = 17\,\mu$m and length $L = 32\,\mu$m, with $\boldsymbol{e}_r$ and $\boldsymbol{e}_x$ unit vectors in the corresponding radial and streamwise directions. $N_c = 8$ model red blood cells of nominal radius $r_o = 2.82\,\mu$m (the radius of a sphere of the same volume) are initiated in their at-rest biconcave geometry (as described elsewhere [5]) and uniformly spaced along the vessel with their symmetry axis aligned with that of the vessel. We confirm that our principal conclusions are insensitive to doubling both L and N_c. The flow in the vessel has mean velocity $U = 2.9 \times 10^2\,\mu$m/s, which is physiologically realistic [29]. The interior cellular (cytosol) and exterior (plasma) fluids are Newtonian with the same viscosity $\mu = 1.2 \times 10^{-3}$ Pas. Actual red blood cells are estimated to have an elevated cytosol viscosity by about a factor of 5 [58–60], yet matched-viscosity models are simpler and have been shown to be sufficient to reproduce microcirculatory phenomenology [9], and to quantitatively reproduce the suspension effective viscosity [28,61].

The red blood cell elastic membrane is described with the commonly used Skalak constitutive model, with independent shear, dilatation, and bending moduli [61]. The shear and bending moduli are $E_s = 4.2 \times 10^{-6}$ N/m and $E_b = 1.8 \times 10^{-19}$ N m, respectively, which are based on experimental

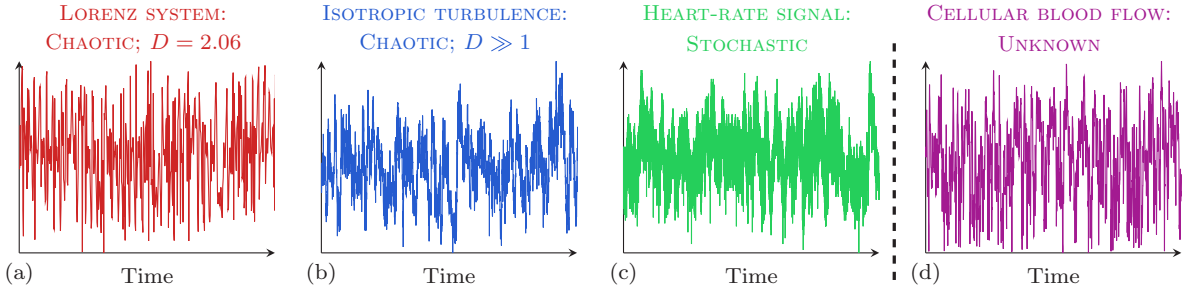

FIG. 2. Examples of different dynamic behaviors: (a) First component of the Lorenz system following Bryant *et al.* [40], (b) streamwise velocity of a fixed location in a turbulent Poiseuille flow [41], (c) tachogram of a supraventricular ectopy [42], and (d) radial centroid position of a flowing model red blood cell, used in this work. Panels (a) and (b) include approximations of the strange attractor dimension D.

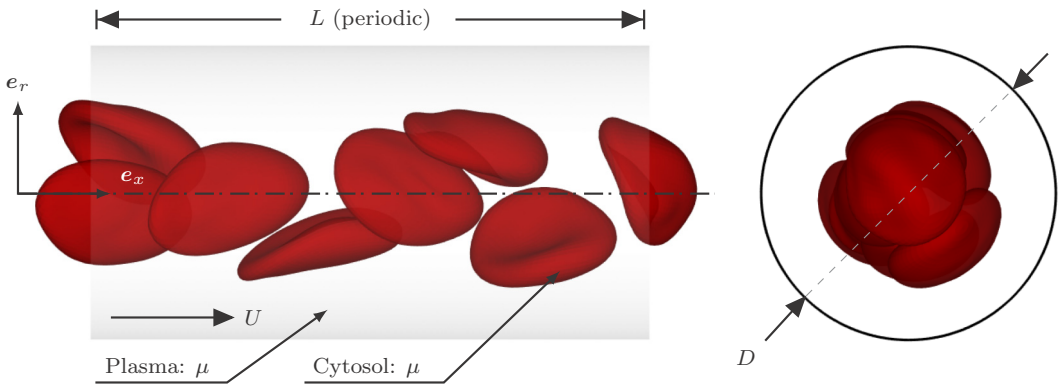

FIG. 3. The model flow system.

measurements [5]. Red-blood-cell membranes are known to be nearly incompressible, which is approximately enforced by a large dilatation modulus $E_d = 67.7 \times 10^{-6}$ N/m.

We focus on the radial centroids of the red cells within the vessel, $\boldsymbol{R} = \{R_1, \ldots, R_{N_c}\}$, as measured from the vessel streamwise-centerline. This is an important quantity when analyzing cellular blood flow, particularly when considering so-called shear-induced migration [62–65], and for designing microfluidic devices for plasma–cell separation [66,67], cell sorting [68,69], and cell-focusing [16]. For the configurations we consider, the initial radial centroid positions $\boldsymbol{R}(t = 0)$ are perturbed by uniformly sampled distances up to $0.1r_o$ in a randomly selected radial and streamwise direction. This is done to accelerate breakdown into the disordered flow we study in detail. However, since the flow is unstable it will eventually become disordered regardless of the specific perturbation [12].

III. NUMERICAL METHOD

Reynolds numbers of microcirculatory flow are typically small, $\mathrm{Re} \equiv \rho U D/\mu \lesssim 0.01$ (where ρ is the fluid density), so inertia is neglected and the flow velocity $\boldsymbol{u}$ is governed by the Stokes equations,

$$-\nabla p + \mu \nabla^2 \boldsymbol{u} = \boldsymbol{0}, \tag{1}$$

with the usual incompressibility constraint $\nabla \cdot \boldsymbol{u} = 0$ enforced by the pressure p. We utilize a standard boundary integral formulation [70–72], for which the velocity is

$$u_i(\boldsymbol{x}_o) = u_i^{\infty}(\boldsymbol{x}_o) - \frac{1}{8\pi\mu} \int_{\Omega} G_{ij}(\boldsymbol{x} - \boldsymbol{x}_o) \Delta\sigma_j(\boldsymbol{x})\, dS(\boldsymbol{x}), \tag{2}$$

for coordinate direction $i = \{1, 2, 3\}$. In Eq. (2), $\boldsymbol{x}_o$ is a point on a cell surface, Ω is the union of all surfaces as shown in Fig. 3, $\Delta\boldsymbol{\sigma}$ is the surface traction on the fluid, and $\boldsymbol{G}$ is the triply periodic Stokes Green's function. Here, $\boldsymbol{u}^{\infty} = \{0, 0, \hat{U}\}$ is the total mean velocity in the periodic rectangular computational domain, where $\hat{U}$ is useful for setting the flow strength. However, $\hat{U}$ does not exactly match U, since there is also flow outside the cylindrical vessel; we compute $U = 1.25\hat{U}$ [61].

The cell membranes $\boldsymbol{x}$ are represented with spherical harmonics, which are advantageous as a relatively small number of spherical harmonic modes are required to accurately describe the cell shape, as well as for facilitating a nondissipative approximate dealiasing method for stabilization [61]. There are M^2 spherical harmonic modes per cell membrane. We use $M = 12$, though three times this amount are carried during each time step for dealiasing [73]. The surface traction is evaluated from the Skalak model using the spherical harmonic expansion.

In our formulation, boundary integrals are evaluated using a quadrature scheme for the collocation points $\vec{\boldsymbol{x}}$ [61]. For close interactions, we switch to a nearly singular formulation of the integrands [61]. The resulting system is approximately evaluated by a particle-mesh-Ewald (PME) algorithm generalized for Stokes flow [61,74].

The vessel wall is represented by 6588 triangular mesh elements. A single-layer potential is used to enforce the no-slip condition by solving for the required surface traction on the wall with a GMRES algorithm [61,75].

Since both the cytosol and plasma are incompressible, there should be no change in cell volume, though errors can accumulate over long times. We correct the cell volume through adjustment of the cell membrane in its normal direction [61]. Reported simulations require adjustments of less than $10^{-5} r_o$ per time step.

Once the velocity $\boldsymbol{u}$ is computed by evaluating Eq. (2), the cell surfaces are advanced according to

$$\frac{d\boldsymbol{x}}{dt} = \boldsymbol{u}(\boldsymbol{x}), \tag{3}$$

which is integrated using a first-order explicit method with time step $\Delta t = 0.0014\, r_o/U$. These numerical parameters have been sufficient to successfully reproduce the effective viscosity of blood flowing in confined tubes such as we consider here [73].

IV. RESULTS

A. Flow kinematics and patterns

1. Long-time flow simulations

First, we simulate the flow of Sec. II until $t = T \equiv 2800 r_o/U$, which corresponds to about 8000 flow-throughs for a typical cell through the streamwise-periodic tube. Figure 4 shows the cell centroid positions $R_j(t)$ for two example cells of the eight total. After the transient period $t \lesssim t_o \equiv 300 U/r_o$ no obvious pattern can be discerned. Thus, we

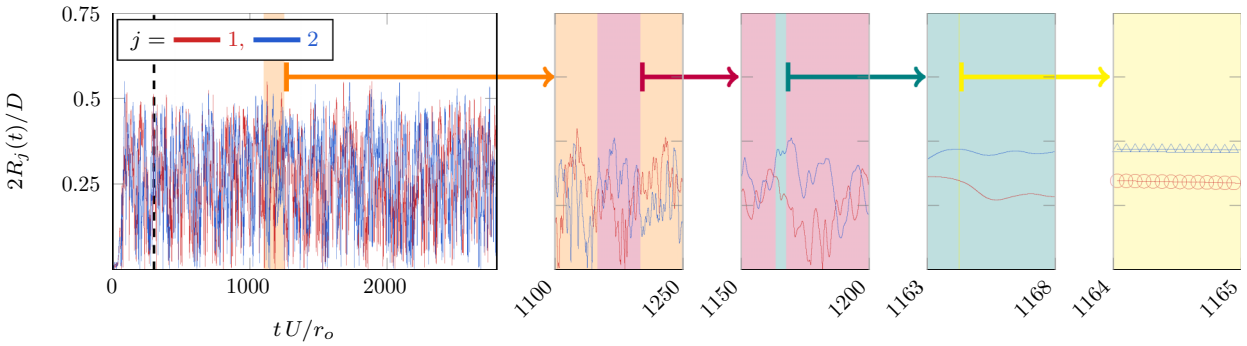

FIG. 4. Radial cell centroid position $R_j(t)$ for example cells $j = 1$ and 2. The symbols indicate numerical time steps. The dashed vertical line marks the start of our sampling, $t = t_o$ (see text).

analyze kinematics for $t > t_o$. The time series data for the jth cell is compactly represented as a column vector $\vec{\boldsymbol{r}}$ whose ith elements are

$$r_i = R_j(t_o + i\Delta t) \quad \text{for} \quad i = 1, \ldots, N_t,\ j = 1, \ldots, N_c, \quad (4)$$

where $N_t = 2 \times 10^6$ is the number of time steps. Indeed, for most analysis, we only require data from one cell, as our principal conclusions are independent of the specific cell observed.

2. Space–time separation

We first construct a space–time separation map to show dynamic correlations, patterns, and coherent structures in the data [76], which are useful tools when considering a reduced-order model for the cell motion. To do this, the data are recast using spatial and temporal separations,

$$\delta_r = |r_j - r_i| \quad \text{and} \quad \delta_t = |j - i|\Delta t, \quad (5)$$

respectively, for which $\delta_t \in (\Delta t, 20r_o/U)$ is sampled uniformly and randomly and $\delta_r(\delta_t)$ is computed 10^6 independent times.

Figure 5 shows the space–time separations of $\vec{\boldsymbol{r}}$ and the cumulative probability $P(\delta_r < X|\delta_t)$ for varying X. As expected, small δ_t ($\lesssim 5r_o/U$ in this case) always corresponds to small δ_r. Importantly, $P(\delta_t)$ is approximately constant for $\delta_t \gtrsim 5r_o/U$. Thus, any recurrent features in $\vec{\boldsymbol{r}}$ (e.g., small δ_r for large δ_t, which has been observed for several low-dimensional chaotic systems [76]) are unclassifiable by this method. While this behavior is similar to that of some stochastic systems (e.g., $1/f$ noise [76] and eye movement dynamics [77]), it is insufficient to distinguish between chaotic and stochastic features. As such, we further analyze the cell kinematics for a lower-order description of the flow.

3. Fourier power spectrum

Next, we consider the frequency-domain representation of our data. A dominant frequency, or a compact set of frequencies, indicates recurrent flow dynamics that can provide a basis for reduced-order modeling [78,79]. While the flow is of course fundamentally recurrent since it is spatially confined, a recurrence associated with a unique frequency can indicate nontrivial low-dimensional dynamics. We compute the discrete Fourier transform $\boldsymbol{F}$ using a Hann windowing function [80] and the time series $\vec{\boldsymbol{r}}$ as

$$F_n(\vec{\boldsymbol{r}}) = \frac{1}{\sqrt{N_t}} \sum_{k=0}^{N_t-1} r_j \exp\left(\frac{2\pi i k n}{N_t}\right) \quad \text{for} \quad n = 0, \ldots, N_t/2-1, \quad (6)$$

where $i \equiv \sqrt{-1}$ is the imaginary unit, $k_n = 2\pi n/T$ is the wave number index, and $\omega_n \equiv k_n r_o/U$ follows as the dimensionless frequency.

Figure 6 shows the power spectrum for the radial cell positions. We observe a power-law behavior for $\omega \gtrsim U/L$, with $\boldsymbol{F}(\vec{\boldsymbol{r}}) \propto \omega^{-8/3}$ being a modestly better fit to the data than $\boldsymbol{F}(\vec{\boldsymbol{r}}) \propto \omega^{-3}$. This slope is distinct from the "flicker"

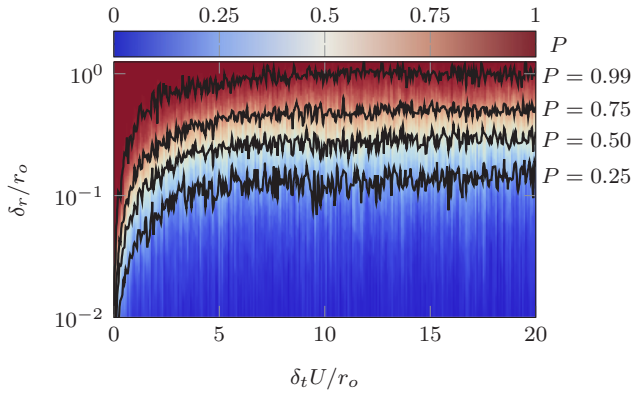

FIG. 5. Space-time separations of $\vec{\boldsymbol{r}}$ and corresponding curves of constant $P(\delta_r < X|\delta_t)$.

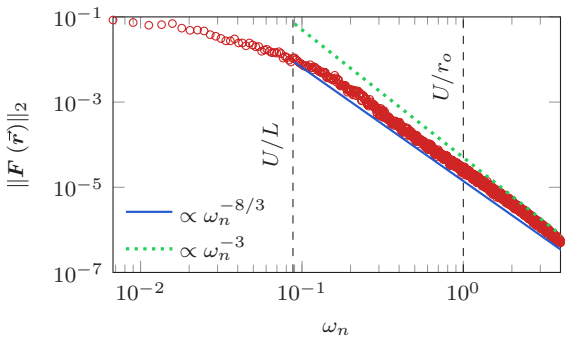

FIG. 6. Fourier spectrum of $\vec{\boldsymbol{r}}$ and frequencies corresponding to U/r_o and U/L as labeled.

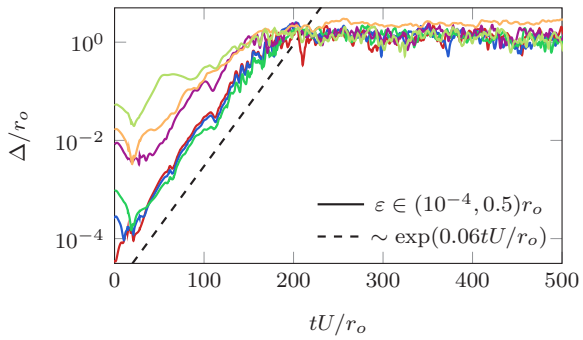

FIG. 7. Radial displacement Δ of cell perturbations to initial configuration $\boldsymbol{R}(t)$ (see text). Magnitudes range from $\varepsilon = 10^{-4} r_o$ to $0.5 r_o$.

or pink $1/\omega$ and Brownian $1/\omega^2$ signatures observed for some physical systems, such as metal films [81], condensed matter electronics [82] and semiconductors [83], and phase transitions [84], and thus cannot be directly connected to these noise processes.

For $\omega \lesssim U/L$ there is no distinct frequency, and so we conclude that the dynamics are sufficiently coupled that their time scales are unidentifiable by this analysis (this does not prohibit recurrent behaviors generally, but rather suggests that they are sufficiently high-dimensional to be inseparable). This property is generally observed for high-dimensional chaotic systems, which presents an additional modeling opportunity that we focus on next.

B. Chaotic properties

1. Sensitivity to initial conditions

We next assess if the flow has chaotic characteristics. Chaotic flows exist in a so-called phase space which, if it can be reconstructed, provides a reduced-order description of the flow. Of course, the dimensionality of the associated phase space limits the reducibility of the dynamics. Here, we determine if the flow can be considered chaotic, and if so, the dimensionality of its associated strange attractor.

The assess the existence of chaotic behaviors by computing the sensitivity of the cell kinematics to perturbations in their initial condition. Here, $\boldsymbol{R}(t)$ are the radial locations of the cell centroids and $\boldsymbol{R}_\varepsilon(t)$ are the radial locations with an additional small displacement at $t = 0$. These are added in a uniformly distributed random direction with uniformly randomized magnitude $\hat{\varepsilon} \in [0, \varepsilon]$. The sensitivity is measured as a nominal distance between these two configurations:

$$\Delta(t) = \|\boldsymbol{R}_\varepsilon(t) - \boldsymbol{R}(t)\|_2, \tag{7}$$

where $\|\cdot\|_2$ is the usual L_2 norm.

Figure 7 shows the sensitivity of the radial centroid positions. The differences Δ initially decay a small amount in some cases, which appears to be due to an initial rapid, though transient, decay in cell-scale perturbations [11]. Afterward, $\Delta(t)$ grows exponentially with $\Delta \sim \exp(\lambda t)$ where λ is between $0.032U/r_o$ and $0.061U/r_o$ for the case we consider here. This measure provides an estimate of the first local Lyapunov exponent [85], for which $\lambda > 0$ indeed indicates chaotic dynamics. We note that the variance associated with the estimation of Lyapunov exponents and their relatively small values means that a certain classification of chaotic behavior is challenging to provide. Thus, we can only state that our approximation of the largest Lyapunov exponent serves as one indication that the flow is chaotic. However, later we will show that this classification is only of tertiary importance when formulating a reduced-order flow model.

After $t \approx 200U/r_o$ the growth saturates at $\Delta \approx r_o$, as expected due to the radial confinement of the flow. This gives a Lyapunov time horizon of $t_c = 614U/r_o$ for an IEEE 64-bit finite-precision error ($\approx 10^{-14}$) to reach unity. Thus, the flow is indeed chaotic. However, in order to utilize this property for a reduced-order representation, the associated strange attractor must have a relatively small dimension [50].

2. Attractor dimension

We use the correlation dimension to estimate D, which is related to the correlations between $\vec{\boldsymbol{r}}$ and the reconstructed attractor. Due to the exponential divergence of trajectories, most pairs (r_i, r_j), with $i \neq j$, will be uncorrelated pairs of seemingly random radial cell locations. The correlation between the $\vec{\boldsymbol{r}}$ and the reconstructed attractor is measured by the correlation integral (though its usual form is presented as a discrete sum [76]), which is the mean probability that discrete states at two different times are within a threshold distance ℓ,

$$C(\ell) = \frac{1}{N_t^2} \sum_{\substack{i,\, j=1 \\ i \neq j}}^{N_t} H(\ell - \|\widetilde{r}_i - \widetilde{r}_j\|_2), \tag{8}$$

where H is the Heaviside step function and

$$\widetilde{r}_i = \{r_i, r_{i+\tau}, \ldots, r_{i+\tau(m-1)}\}, \tag{9}$$

is the time-delay embedding of $\vec{\boldsymbol{r}}$, as parameterized by its embedding dimension m and time delay τ [86]. If for small ℓ, $C(\ell)$ has a power law behavior,

$$C(\ell) \sim \ell^v, \tag{10}$$

then v is called the correlation dimension, which serves as a measure of the local structure of an attractor. If $v = m$, then the embedding dimension is not sufficiently large to determine the attractor dimension. We compute the correlation dimension v of Eq. (10) as

$$v(\ell) = \frac{d \log C(\ell)}{d \log \ell}. \tag{11}$$

The correlation integral of $\vec{\boldsymbol{r}}$ is shown in Fig. 8(a). For $\ell \lesssim 4 \times 10^{-3} r_o$ the correlation dimension matches the embedding dimension with $C(\ell) \sim \ell^m$, and so m is not large enough to discern an attractor dimension. A "knee" in $C(\ell)$ is seen for $4 \times 10^{-3} \lesssim \ell \lesssim 0.03$ and $m > 3$, where $v(\ell) \approx 1$. In the knee region the data are too close in the reconstructed phase space to serve as an estimate the correlation integral, a result also seen for stationary stochastic processes with a power-law spectrum [76,87] and some low-dimensional chaotic systems (e.g., pulsar spin-down rates [88]). Thus, we label $0.03 < \ell < 1$ as a realizable scaling region, where we estimate a power-law behavior in ℓ. We note that while $v(\ell) < m$ in this region, this is not the usual observed behavior and it is possible that no robust scaling region exists [76]. If this is

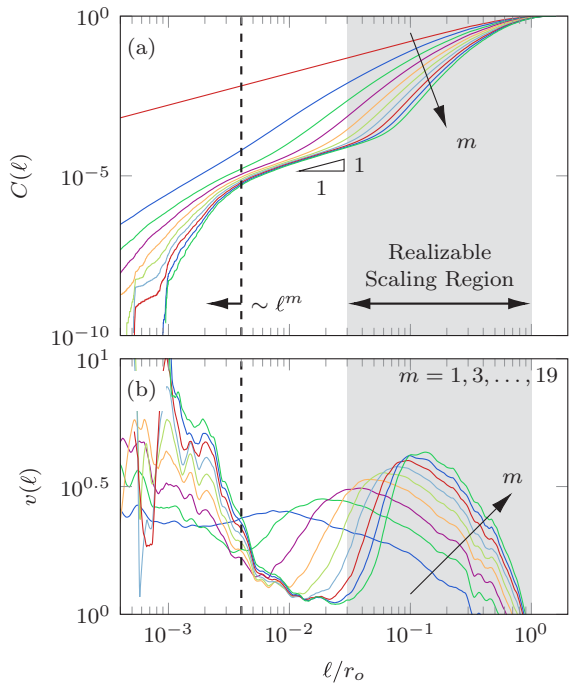

FIG. 8. (a) Correlation integral $C(\ell)$ from Eq. (8), (b) correlation dimension $v(\ell)$ from Eq. (11).

the case, then the correlation dimension is too large to be estimated from $\vec{r}$ and thus traditional attractor reconstruction is prohibitive regardless.

The correlation dimension $v(\ell)$ and its maximum value in the realized scaling region are shown in Fig. 8(b) and Fig. 9, respectively. In this region we have $v < m$, though v still increases with m. Specifically, we have $\max_\ell v(\ell) \sim m^{0.3}$. Also shown is the Kaplan–Yorke dimension:

$$D_{\mathrm{KY}} = j + \frac{1}{|\lambda_{j+1}|}\sum_{i=1}^{j}\lambda_i, \tag{12}$$

where λ_i are the Lyapunov characteristic exponents as computed using the methods of Sano and Sawada [89] and j is the number of nonnegative exponents. The expected inequality $D_{KY} > v$ holds for all computed m [76], and we generally see $D_{\mathrm{KY}} \sim m^{0.3}$.

The monotonically increasing $\max_\ell v(\ell)$ and D_{KY} with m for at least up to $m = 100$, with $D = 6.1$ for this m, suggest

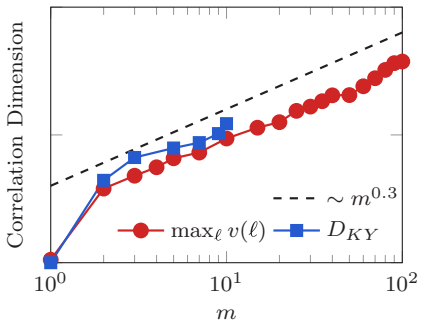

FIG. 9. Maximum correlation dimension in the tentative scaling region (see text) and Kaplan–Yorke dimension D_{KY} for a range of m.

it will not terminate at a fixed value for still larger embedding dimensions. Further, reliable estimation of $D > \log_{10}(N_t) \approx 6$ is prohibitive without larger N_t [49]. However, these dimensions are already sufficiently large to preclude a reduced-order model based upon attractor reconstruction. Given the stochasticlike features of the data, we next explore this property as a potential model for representing the flow statistics.

3. Distinguishing chaos from stochasticity

High-dimensional chaotic flows can often be accurately represented by a stochastic system [46,56], including some turbulent fluid flows [90]. Stochastic process flow states are decided probabilistically, with the associated probabilities computed via simulation data. Given the stochastic features of the correlation integral of Sec. IV B 2, we attempt to more reliably determine if the cellular flow observables can be classified as stochastic. For this, we utilize the structure function as an indicator of chaotic and stochastic behaviors; it is defined as

$$S_{k,m}(n) = \sum_{i=1}^{N_t-n} \left\| d_t^m(r_{i+n} - r_i) \right\|_k, \quad n = 1, \ldots, N_t, \tag{13}$$

where

$$\|\cdot\|_k \equiv \left(\sum_{i=1}^{N_t} |\cdot|^k\right)^{1/k} \tag{14}$$

is the L_k norm, n is the time delay, and d_t^m is m successive applications of the first-order explicit time derivative operator. However, we confirm that the results presented are independent of this choice of derivative operator. Chaotic systems have power-law behavior

$$S_{k,m}(n) \sim n^k, \tag{15}$$

as $n \to 1$ [91–93], while any correlation with n disappears for stochastic systems with increasing m [76].

Figure 10 shows $S_{k,m}$ for both $k = 1$ and 2, following usual practice [76,92,93]. For both k, $S_{k,m}(n) \sim n^k$ for $n \lesssim 50$ and $m = 0$ and 1, indicative of chaos. For $n \gtrsim 200$ $S(n)$ is constant, as expected, due to the finite extent of the phase space. The transition between these two regimes appears nonlinear, indicating a multifractal behavior [94], and thus coupled fractal states [95,96]. Indeed, this is typical of other high-dimensional flow systems, such as turbulence [97–99]. For the flowing red blood cells we consider, we anticipate that the high-dimensional chaotic trajectories identified in the previous subsections lead to this behavior. For increasing time derivatives m, the $n \lesssim 50$ correlation disappears. This is an indicator of stochastic-like features, which thus entails stochastic elements for reduced-order modeling [100].

C. Stochastic modeling

The stochastic features we identify, along with the previous success of stochastic models for high-dimensional flow physics [56,90], suggest that such a model is appropriate for the flow kinematics. Thus, we adopt a stochastic modeling approach to reproduce the features of the flow of Sec. IV A. Here, we classify the relevant stochastic features of the flow

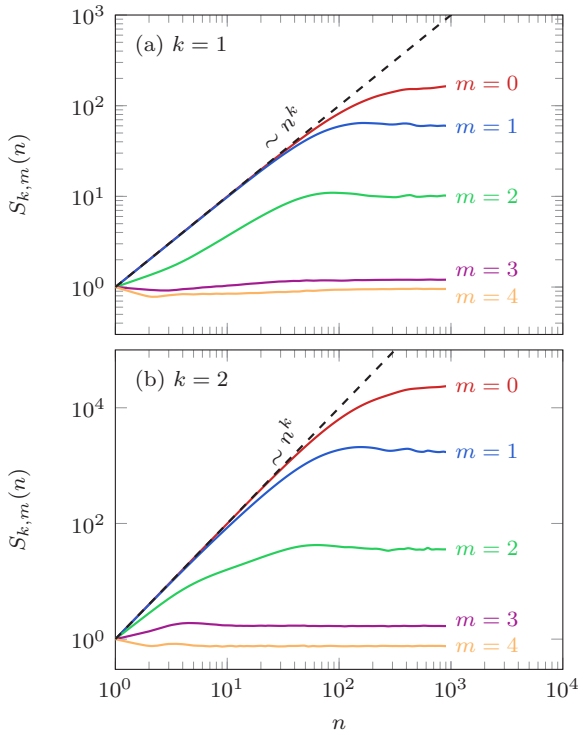

FIG. 10. The structure function for time derivatives $m = 0, 1, \ldots, 4$ and norms (a) $k = 1$ and (b) $k = 2$.

such that a faithful stochastic model can be developed, then train a model and validate it against untrained data.

1. Stationary processes

Stochastic models are generally developed for either stationary processes, whose mean and variance are time independent, or nonstationary processes that do not have this property. Thus, we first determine if the flow is statistically stationary before proceeding with model development. Figure 11 shows the windowed mean and variance of $\vec{\boldsymbol{r}}$; they are both irregular but do not appear to drift. To determine this feature explicitly, the probability that the data are stationary is computed via an augmented Dickey–Fuller test, which determines if the characteristic polynomial of the data has a unity root [102]; stable systems without unit roots are deemed stationary. The table of Fig. 11(b) shows the results of the Phillips–Perron test, where p is the probability of nonstationary behavior (thus, $p = 0$ indicates certainty of stationarity). We observe small p values for all unit root tests, and so we are confident that the process can be modeled accurately as stationary.

2. Markov chain reduced-order model

We will use a Markov chain model to represent the flow $\vec{\boldsymbol{r}}$. Markov chains are a stochastic model that utilizes the probability of transitions between identified flow states. The modeled flow process is every τth component of the evolving radial cell locations $\vec{\boldsymbol{r}}$; we choose $\tau = 50$, which is guided by the space-time separations of Sec. IV A 2, though we confirm that our conclusions are insensitive to doubling of this value. Each iteration of the flow j is in one of $N_p = 20$ unique states $i, r_{j\tau} \in \mathcal{S}_i$, as defined by a uniform discretization of the radial coordinate:

$$\mathcal{S}_i \equiv (s_i, s_{i-1}), \quad \text{where} \quad s_i = \frac{iD}{2N_p r_o} \quad \text{for} \quad i = 1, \ldots, N_p. \tag{16}$$

While this formulation is simple, identifying states via a more sophisticated K-means algorithm did not provide better agreement [103]. The model flow $\vec{\boldsymbol{r}}^M$ is defined by the transition matrix P_{ij}, which is the probability that $\vec{\boldsymbol{r}}$ switches from $\mathcal{S}_i$ to $\mathcal{S}_j$ after one process iteration; it also has the property

$$\sum_{j=1}^{N_p} P_{ij} = 1 \quad \text{for} \quad i = 1, \ldots, N_p. \tag{17}$$

A temporal training window $\Omega_t \in (tU/r_o = t_o, 1575)$ of $\vec{\boldsymbol{r}}$ is used to compute $\boldsymbol{P}$, and untrained data $t \notin \Omega_t$ is used for validation. We compute $\boldsymbol{P}$ using the training window portion of $\vec{\boldsymbol{r}}$ iteratively over each state i as

$$P_{ik} \leftarrow P_{ik} + \delta_{j,k}\Delta P - (1 - \delta_{j,k})\frac{\Delta P}{N_p - 1} \quad \text{for} \quad k = 1, \ldots, N_p, \tag{18}$$

where $\Delta P = 1/i$ and $\delta_{j,k}$ is the Kronecker symbol.

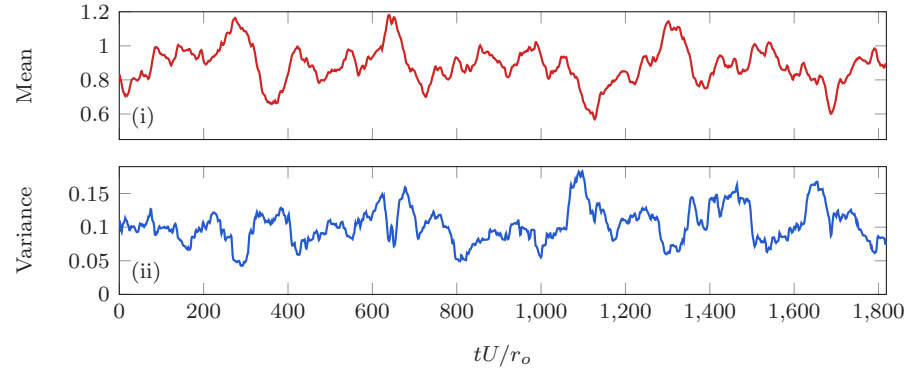

(a)

Test	Cell	p-value
PP (F)	1	0.00694
PP (t)	1	0.00622
PP (F)	2	0.00252
PP (t)	2	0.00256
PP (F)	3	0.00386
PP (t)	3	0.00366

(b)

FIG. 11. (a) Windowed (i) mean and (ii) variance computations for $\vec{\boldsymbol{r}}$, with window length $\Delta t_{\text{win.}} = 1000U/r_o$. (b) The results of a Phillips–Perron (PP), or augmented Dickey–Fuller, test for the cell data indicated based upon F and t metrics (see Elder and Kennedy [101]).

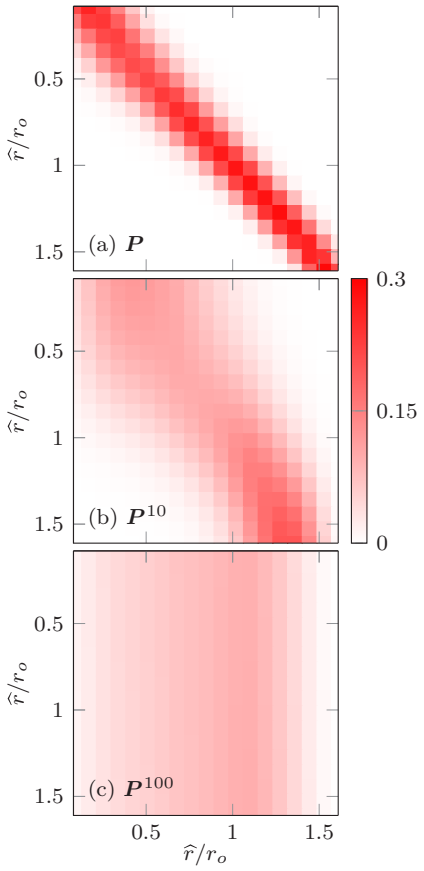

FIG. 12. (a) Transition matrix $\boldsymbol{P}$ and its products (b) $\boldsymbol{P}^{10}$ and (c) $\boldsymbol{P}^{100}$ as labeled. Axis values $\widehat{r}$ are scaled with the s_i of Eq. (16) and r_o to give the radial coordinate of the corresponding state.

Figure 12(a) shows that $\boldsymbol{P}$ is only nonzero near the diagonal. Thus, a state is most likely to transfer to itself or its nearest neighbors. Matrix–matrix products of $\boldsymbol{P}$ are shown in Figs. 12(b) and 12(c); for $\boldsymbol{P}^{10}$ we see the diagonal components are smeared nonuniformly across nearly the full range of states, with the largest components being in the bottom-right portion of the matrix, suggesting more complex dynamics in this limit. An apparent steady state is reached by $\boldsymbol{P}^{100}$, which is vertically banded.

The connections indicated by the iterated transition matrix $\boldsymbol{P}^5$ are illustrated in Fig. 13. We see that dynamics are complex, as was implied by Fig. 12. There are self-reinforcing feedback loops for clusters 1–5 and 7–10, indicating a circular transition between the states. Since these clusters are for neighboring state numbers, cells near the tube centerline are generally more likely to stay there than to flow towards the wall, though their exact motion while near the tube center is relatively complicated, as indicated by the network of connections joining clusters 1–5. Similar behavior is observed for cells flowing nearer the vessel wall; the cells are more likely to stay far from the tube center than to flow near it, though their specific motion is complex, as indicated by the neighboring connections between clusters 7–10. More important, however, is the ability of the associated transition matrix to reproduce the statistics of the model flow, which we consider next.

3. Stochastic model flow

The model flow $\vec{\boldsymbol{r}}^M$ is generated from $\boldsymbol{P}$ using

$$r^M_{\tau(i+1)} = \boldsymbol{P} r^M_{\tau i} \qquad \text{for } i = 1, \ldots, N_t/\tau. \tag{19}$$

The full and model flows within a temporal verification window are shown in Fig. 14; the time series have qualitatively similar irregularities, though since the flow is chaotic, we cannot hope to predict $\vec{\boldsymbol{r}}$ exactly. Instead, we analyze the statistics of the model and full flows. For this, we first compute the eigenvalue decomposition of $\boldsymbol{P}$ as

$$\boldsymbol{P}^\top = \boldsymbol{S}\boldsymbol{\Lambda}\boldsymbol{S}^{-1}, \tag{20}$$

where $\boldsymbol{P}^\top$ is the transpose of $\boldsymbol{P}$, $\boldsymbol{S}$ is the column matrix of left eigenvectors, and $\boldsymbol{\Lambda}$ is the real-ordered diagonal matrix of eigenvalues. For the Markov process Eq. (19), the left eigenvectors $\boldsymbol{S}$ are statistically invariant distributions that can indicate recurring flow processes not identified via Fourier analysis [104,105].

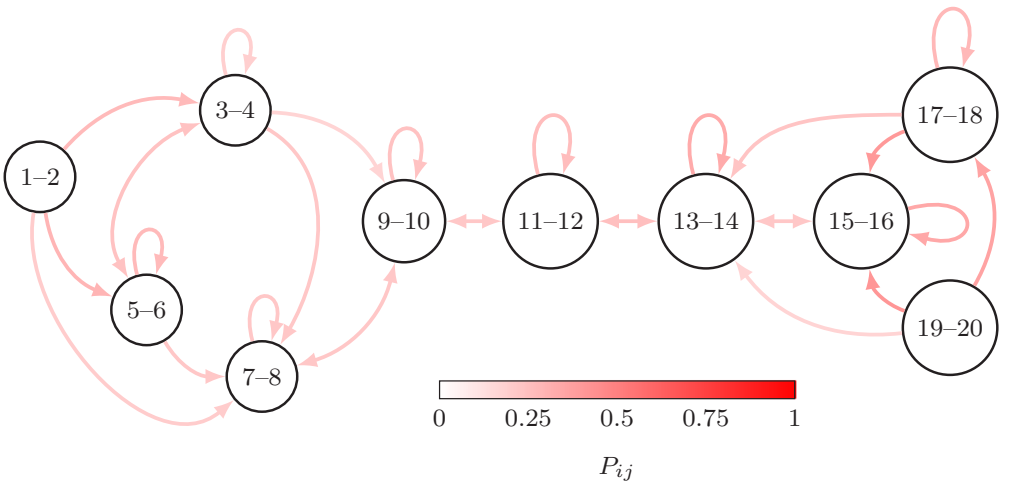

FIG. 13. The three most probable transitions of $\boldsymbol{P}^5$. The numbers indicate the state index $\mathcal{S}_i$, where neighboring states have been coalesced for visualization purposes, and thus the transitions between them are not shown.

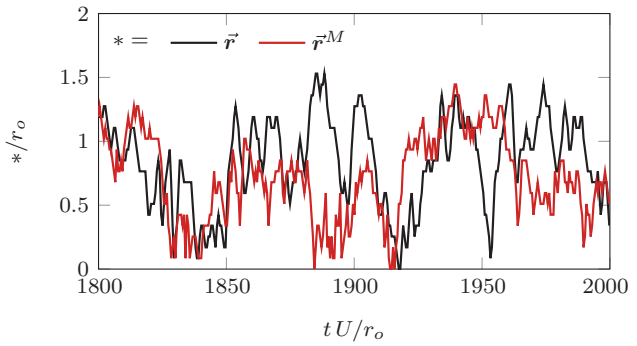

FIG. 14. The full ($\vec{r}$) and model ($\vec{r}^M$) flows within the verification window $\Omega_v \in (tU/r_o = 1800, 2000)$.

In Fig. 15(a) we see that the model flow is able to reproduce the PDF of the full flow. Further, the PDF of $\boldsymbol{S}_1$ also matches that of the model flow, so the first eigenmode of $\boldsymbol{P}$ dominates the mean statistics. The PDFs of the first three eigenvectors are shown in Fig. 15(b). We see that the PDFs of $\boldsymbol{S}_2$ and $\boldsymbol{S}_3$ exhibit two and three subdomains, respectively, indicating the propensity of flow states to transition to only nearby states, a behavior also observed in the graph of Fig. 13 for clusters 1–5 and 7–10; as discussed above, this is associated with the higher likelihood that cells near the tube centerline will stay there (and vice-versa for cells flowing near the vessel wall). To quantitatively assess the statistical validity of our model, we compare the moments of the PDFs of the full and model flows. The ith moment of a discrete distribution $\vec{v}$ of length N is computed as

$$M_i(\vec{v}) = \frac{1}{N}\sum_{j=1}^{N}(v_j - \bar{v})^i, \quad \text{where} \quad \bar{v} = \frac{1}{N}\sum_{j=1}^{N} v_j \tag{21}$$

is the mean.

Table I shows the first five moments of the PDFs of the flows. We see that the relative error between corresponding moments is less than 10% for all moments shown, with the error increasing with increasing moment number. This relatively small error serves as a demonstration of the ability

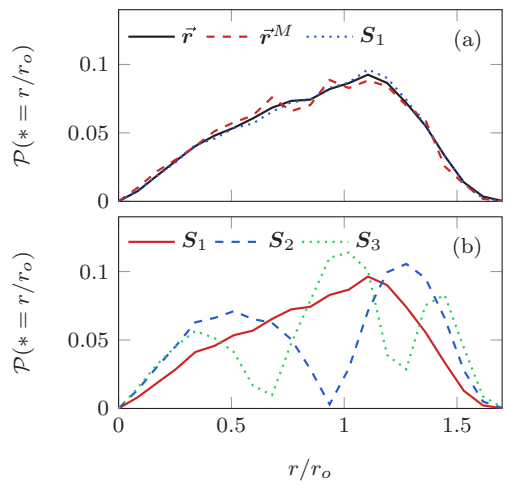

FIG. 15. PDF $\mathcal{P}(\cdot)$ of (a) model flow $\vec{r}^M$, full flow $\vec{r}$, and the first left eigenvector $\boldsymbol{S}_1$, and (b) the first three left eigenvectors of $\boldsymbol{P}^\top$.

TABLE I. The first five moments of $\mathcal{P}(\vec{r})$ and $\mathcal{P}(\vec{r}^M)$, and the relative error between them. The percentage error is computed as $\%_{\text{error}} \equiv 100\{M_i[\mathcal{P}(\vec{r}^M)] - M_i[\mathcal{P}(\vec{r})]\}/M_i[\mathcal{P}(\vec{r})]$.

$M_i(*)$	$i=1$	2	3	4	5
$\mathcal{P}(\vec{r})$	0.817	0.788	0.831	0.929	1.081
$\mathcal{P}(\vec{r}^M)$	0.795	0.753	0.782	0.858	0.981
$\%_{\text{error}}$	2.76	4.52	5.97	7.60	9.21

of a relatively simple Markov chain model with few degrees of freedom to statistically reproduce the features of flowing red blood cells.

V. DISCUSSION AND CONCLUSIONS

Our goal was to analyze and classify the kinematics of cellular blood flow to facilitate the design of reduced-order models. We first attempted to uncover any basic flow recurrences. Long-time flow separations were analyzed via a space-time separation map, which showed that only trajectories that were nearby in time were likely to be nearby in space; thus, no spatial recurrences were identified. The flow was analyzed in the frequency domain using a Fourier decomposition of the time-series data. The Fourier spectrum appeared relatively flat for small frequencies, and so there was no dominant flow frequency but rather a complex set of coupled flow frequencies.

Given the irregular character of the flow, a lower-dimensional strange attractor was sought to describe it. For this, we prescribed small perturbations to the initial flow configuration and tracked their divergence. A strange attractor was found to exist, though by our analysis its dimension was relatively large, with $D > 6$ for embedding dimension $m = 100$. As a result, the flow could not be described with just a few degrees of freedom, and the usual techniques, such as Poincaré maps, could not be utilized to further analyze the chaotic behavior or reconstruct the attractor. However, we did see that the chaotic dimension of the flow was sufficiently large to exhibit stochastic-like features. Given this, we utilized a structure function to show that the cell kinematics were indistinguishable from those generated by a stochastic process.

Based upon this stochasticity, a reduced-order statistical model was formulated for the radial cell positions based upon Markov chains. The Markov chain transition matrix was computed with only $N_p = 20$ Markov states. A graph of the most probable cluster transitions revealed two main groups of clusters that had self-reinforcing feedback loops, which indicated regular transitions between these nearby states. Physically, this was associated with the propensity for cells near the tube center to stay there, with relatively small probability of moving toward the vessel wall. The model flow was generated from the transition matrix over a temporal verification window. Ultimately, the reduced-order model flow was shown to closely predict the statistics of the full flow via comparisons between their associated PDFs and higher-order moments. Of course, increasing the number of Markov states will improve model accuracy and require less interpolation between adjacent states. Further, other modeling options are available, such as the interpolative models associated with

machine learning techniques. However, we did not explore those here in the interest of keeping the model simple and the associated flow physics easy to interpret.

ACKNOWLEDGMENT

This work was supported in part by the National Science Foundation under Grant No. CBET 13-36972.

[1] J. H. Barbee and G. R. Cokelet, Prediction of blood flow in tubes with diameters as small as 29 microns, Microvasc. Res. **3**, 17 (1971).

[2] A. R. Pries, T. W. Secomb, and P. Gaehtgens, Biophysical aspects of blood flow in the microvasculature, Cardiovasc. Res. **32**, 654 (1996).

[3] C. Migliorini, Y. Qian, H. Chen, E. Brown, R. Jain, and L. Munn, Red blood cells augment leukocyte rolling in a virtual blood vessel, Biophys. J. **83**, 1834 (2002).

[4] R. D. Kamm, Cellular fluid mechanics, Annu. Rev. Fluid Mech. **34**, 211 (2002).

[5] C. Pozrikidis, Axisymmetric motion of a file of red blood cells through capillaries, Phys. Fluids **15**, 031503 (2005).

[6] A. R. Pries and T. W. Secomb, Chapter 1: Blood flow in microvascular networks, in *Microcirculation*, 2nd ed., edited by R. F. Tuma, W. N. Durán, and K. Ley (Academic Press, 2008), pp. 3–36.

[7] R. Skalak and P. I. Branemark, Deformation of red blood cells in capillaries, Science **164**, 717 (1969).

[8] T. W. Secomb, R. Skalak, N. Ozkaya, and J. F. Gross, Flow of axisymmetric red blood cells in narrow capillaries, J. Fluid Mech. **163**, 405 (1986).

[9] J. B. Freund and M. M. Orescanin, Cellular flow in a small blood vessel, J. Fluid Mech. **671**, 466 (2011).

[10] J. L. McWhirter, H. Noguchi, and G. Gompper, Ordering and arrangement of deformed red blood cells in flow through microcapillaries, New J. Phys. **14**, 085026 (2012).

[11] S. H. Bryngelson and J. B. Freund, Capsule-train stability, Phys. Rev. Fluids **1**, 033201 (2016).

[12] S. H. Bryngelson and J. B. Freund, Global stability of flowing red blood cell trains, Phys. Rev. Fluids **3**, 073101 (2018).

[13] J. L. M. Poiseuille, Recherches sur les causes du mouvement du sang dans les vaisseaux capillaires, CR Acad. Sci. Paris **1**, 554 (1835).

[14] J. Hunter, *A Treatise on the Blood, Inflammation, and Gun-shot Wounds* (Haswell, Barrington, and Haswell, Philadelphia, 1840).

[15] C. Galligan, J. Nichols, E. Kvam, P. Spooner, R. Gettings, L. Zhu, and C. M. Puleo, Mesoscale blood cell sedimentation for processing milliliter sample volumes, Lab. Chip. **15**, 3274 (2015).

[16] N. Xiang and Z. Ni, High-throughput blood cell focusing and plasma isolation using spiral inertial microfluidic devices, Biomed. Microdevices **17**, 110 (2015).

[17] N. S. Dey, S. Majumdar, and M. E. B. Rao, Multiparticulate drug delivery systems for controlled release, Trop. J. Pharm. Res. **7**, 1067 (2008).

[18] F. Lim, *Biomedical Applications of Microencapsulations*, 1st ed. (CRC, Boca raton, FL, 1984).

[19] N. Paret, A. Trachsel, D. L. Berthier, and A. Herrmann, Controlled release of encapsulated bioactive volatiles by rupture of the capsule wall through the light-induced generation of a gas, Chem. Int. Ed. **54**, 2275 (2015).

[20] X. Zhang, W. Wang, W. Yu, Y. Xie, X. Zhang, Y. Zhang, and X. Ma, Development of an in vitro multicellular tumor spheroid model using microencapsulation and its application in anticancer drug screening and testing, Biotechnol. Progr. **21**, 1289 (2005).

[21] W. Kalow, U. B. Meyer, and R. F. Tyndale, *Pharmacogenomics* (CRC Press, Boca Raton, FL, 2001).

[22] T. M. Chang, Blood replacement with nanobiotechnologically engineered hemoglobin and hemoglobin nanocapsules, Wiley Intersci. Rev. Nanomed. Nanobiotechnol. **2**, 418 (2010).

[23] N. Doshi, A. S. Zahr, S. Bhaskar, J. Lahann, and S. Mitragotri, Red blood cell-mimicking synthetic biomaterial particles, Proc. Natl. Acad. Sci. USA **106**, 21495 (2009).

[24] W. M. Kuhtreiber, R. P. Lanza, and W. L. Chick, *Cell Encapsulation Technology and Therapeutics* (Birkhauser, Basel, 1998).

[25] H. A. Clayton, R. F. L. James, and N. J. M. London, Islet microencapsulation: A review, Acta Diabetol. **30**, 181 (1993).

[26] S. Sakai, T. Ono, H. Ijima, and K. Kawakami, Synthesis and transport characterization of alginate/aminopropylsilicate/alginate microcapsule: Application to bioartificial pancreas, Biomaterials **22**, 2827 (2001).

[27] C. A. Taylor and M. T. Draney, Experimental and computational methods in cardiovascular fluid mechanics, Annu. Rev. Fluid Mech. **36**, 197 (2004).

[28] J. B. Freund, Numerical simulations of flowing blood cells, Annu. Rev. Fluid Mech. **46**, 67 (2014).

[29] A. S. Popel and P. C. Johnson, Microcirculation and hemorheology, Annu. Rev. Fluid Mech. **37**, 43 (2005).

[30] G. R. Cokelet, *The Rheology of Human Blood* (Prentice-Hall, Upper Saddle River, NJ, 1972).

[31] A. S. Popel, S. A. Regirer, and P. I. Usick, A continuum model of blood flow.Biorheology **11**, 427 (1974).

[32] J. M. Higgins, D. T. Eddington, S. N. Bhatia, and L. Mahadevan, Statistical dynamics of flowing red blood cells by morphological image processing, PLoS Comput. Biol. **5**, 1 (2009).

[33] T. Mullin, Y. Li, C. Del Pino, and J. Ashmore, An experimental study of fixed points and chaos in the motion of spheres in a Stokes flow, IMA J. App. Math. **70**, 666 (2005).

[34] I. M. Jánosi, T. Tél, D. E. Wolf, and J. A. C. Gallas, Chaotic particle dynamics in viscous flows: The three-particle Stokeslet problem, Phys. Rev. E **56**, 2858 (1997).

[35] J. Dasan, T. R. Ramamohan, A. Singh, and P. R. Nott, Stress fluctuations in sheared Stokesian suspensions, Phys. Rev. E **66**, 021409 (2002).

[36] H. Aref, Stirring by chaotic advection, J. Fluid Mech. **143**, 1 (1984).

[37] H. Aref and S. Balachandar, Chaotic advection in a Stokes flow, Phys. Fluids **29**, 3515 (1986).

[38] J. Chaiken, R. Chevray, M. Tabor, and Q. M. Tan, Experimental study of Lagrangian turbulence in a Stokes flow, Proc. R. Soc. Lond. A **408**, 165 (1986).
[39] J. Chaiken, C. K. Chu, M. Tabor, and Q. M. Tan, Lagrangian turbulence and spatial complexity in a Stokes flow, Phys. Fluids **30**, 687 (1987).
[40] P. Bryant, R. Brown, and H. D. I. Abarbanel, Lyapnunov Exponents from Observed Time Series, Phys. Rev. Lett. **65**, 1523 (1990).
[41] H. Kang, S. Chester, and C. Meneveau, Decaying turbulence in an active-grid-generated flow and comparisons with large-eddy simulation, J. Fluid Mech. **480**, 129 (2003).
[42] A. L. Goldberger, L. A. N. Amaral, L. Glass, J. M. Hausdorff, P. Ch. Ivanov, R. G. Mark, J. E. Mietus, G. B. Moody, C.-K. Peng, and H. E. Stanley, PhysioBank, PhysioToolkit, and PhysioNet: Components of a new research resource for complex physiologic signals, Circulation **101**, E215 (2000).
[43] M. J. McGuinness, The fractal dimension of the Lorenz attractor, Phys. Lett. A **99**, 5 (1983).
[44] P. Cvitanović, R. Artuso, R. Mainieri, G. Tanner, and G. Vattay, *Chaos: Classical and Quantum* (Niels Bohr Institute, Copenhagen, 2016).
[45] F. Takens, Detecting strange attractors in fluid turbulence, in *Dynamical Systems and Turbulence*, edited by D. Rand and L. S. Young, Lecture Notes in Mathematics, Vol. 898 (Springer–Verlag, Berlin, 1981), pp. 366–381.
[46] M. Casdagli, Chaos and deterministic versus stochastic nonlinear modelling, J. R. Stat. Soc. Series B: Methodol. **54**, 303 (1992).
[47] A. Brandstater and H. L. Swinney, Strange attractors in weakly turbulent Couette–Taylor flow, Phys. Rev. A **35**, 2207 (1987).
[48] L. Keefe, P. Moin, and J. Kim, The dimension of attractors underlying periodic turbulent Poiseuille flow, J. Fluid Mech. **242**, 1 (1992).
[49] D. Ruelle, The Claude Bernard lecture, 1989 - deterministic chaos: the science and the fiction, Proc. Roy. Soc. London. A. Math. Phys. Sci. **427**, 241 (1989).
[50] L. M. Pecora, L. Moniz, J. Nichols, and T. L. Carroll, A unified approach to attractor reconstruction, Chaos **17**, 013110 (2007).
[51] D. J. Thomson, Criteria for the selection of stochastic models of particle trajectories in turbulent flows, J. Fluid Mech. **180**, 529 (1987).
[52] M. Strumik and W. M. Macek, Testing for Markovian character and modeling of intermittency in solar wind turbulence, Phys. Rev. E **78**, 026414 (2008).
[53] S. Kimiagar, M. Sadegh Movahed, S. Khorram, and M. Reza Rahimi Tabar, Markov properties of electrical discharge current fluctuations in plasma, J. Stat. Phys. **143**, 148 (2011).
[54] F. Shayeganfar, S. Jabbari-Farouji, M. Sadegh Movahed, G. R. Jafari, and M. Reza Rahimi Tabar, Stochastic qualifier of gel and glass transitions in laponite suspensions, Phys. Rev. E **81**, 061404 (2010).
[55] R. Stresing, J. Peinke, R. E. Seoud, and J. C. Vassilicos, Defining a New Class of Turbulent Flows, Phys. Rev. Lett. **104**, 194501 (2010).
[56] R. Friedrich, J. Peinke, M. Sahimi, and M. Reza Rahimi Tabar, Approaching complexity by stochastic methods: From biological systems to turbulence, Phys. Rep. **506**, 87 (2011).
[57] C. E. Leith, Stochastic models of chaotic systems, Physica D **98**, 481 (1996).
[58] J. D. Bronzino, *The Biomedical Engineering Handbook* (IEEE Press/CRC Press, Boca Raton, FL, 2000).
[59] R. L. Whitmore, *Rheology of the Circulation* (Pergamon, Oxford, 1968).
[60] L. Distenfass, Internal viscosity of the red cell and a blood viscosity equation, Nature **219**, 956 (1968).
[61] H. Zhao, A. H. G. Isfahani, L. Olson, and J. B. Freund, A spectral boundary integral method for micro-circulatory cellular flows, J. Comp. Phys. **229**, 3726 (2010).
[62] J. B. Freund, Leukocyte margination in a model microvessel, Phys. Fluids **19**, 023301 (2007).
[63] J. C. Firrell and H. H. Lipowsky, Leukocyte margination and deformation in mesenteric venules of ram, Am. J. Physiol. Heart Circ. Physiol. **225**, 1667 (1989).
[64] R. G. Henríquez Rivera, K. Sinha, and M. D. Graham, Margination Regimes and Drainage Transition in Confined Multicomponent Suspensions, Phys. Rev. Lett. **114**, 188101 (2015).
[65] R. Skalak, N. Ozkaya, and T. C. Skalak, Biofluid mechanics, Annu. Rev. Fluid Mech. **21**, 167 (1989).
[66] M. Faivre, M. Abkarian, K. Bickraj, and H. A. Stone, Geometrical focusing of cells in a microfluidic device: An approach to separate blood plasma, Biorheology **43**, 147 (2006).
[67] X. Chen, C. C. Liu, and H. Li, Microfluidic chip for blood cell separation and collection based on crossflow filtration, Sensors and Actuators B: Chemical **130**, 216 (2008).
[68] M. Toner and D. Irimia, Blood-on-a-chip, Ann. Rev. Biomed. Eng. **7**, 77 (2005).
[69] J. Kim, M. Massoudi, J. F. Antaki, and A. Gandini, Removal of malaria-infected red blood cells using magnetic cell separators: A computational study, Appl. Math. Comput. **218**, 6841 (2012).
[70] S. Kim and S. J. Karrila, *Microhydrodynamics: Principles and Selected Applications* (Butterworth-Heinemann, Boston, 1991).
[71] C. Pozrikidis, *Boundary Integral and Singularity Methods for Linearized Viscous Flow* (Cambridge University Press, Cambridge, 1992).
[72] J. M. Rallison and A. Acrivos, A numerical study of the deformation and burst of a viscous drop in an extensional flow, J. Fluid Mech. **89**, 191 (1978).
[73] J. B. Freund and H. Zhao, A fast high-resolution boundary integral method for multiple interacting blood cells, in *Hydrodynamics of Capsules and Biological Cells*, edited by C. Pozrikidis (Chapman and Hall/CRC, Boca Raton, FL, 2010), pp. 71–111.
[74] D. Saintillan, E. Darve, and E. S. G. Shaqfeh, A smooth particle-mesh ewald algorithm for Stokes suspension simulations: The sedimentation of fibers, Phys. Fluids **17**, 033301 (2005).
[75] Y. Saad and M. Schultz, A generalized minimal residual algorithm for solving nonsymmetric linear systems, SIAM J. Sci. Stat. Comput. **7**, 856 (1985).
[76] A. Provenzale, L. A. Smith, R. Vio, and G. Murante, Distinguishing between low-dimensional dynamics and randomness in measured time series, Physica D **58**, 31 (1992).
[77] K. Harezlak and P. Kasprowski, Searching for chaos evidence in eye movement signals, Entropy **20**, 32 (2018).

[78] H. D. I. Abarbanel, R. Brown, J. J. Sidorowich, and L. Sh. Tsimring, The analysis of observed chaotic data in physical systems, Rev. Mod. Phys. **65**, 1331 (1993).

[79] F. M. Izrailev, Simple models for quantum chaos: Spectrum and eigenfunctions, Phys. Rep. **196**, 299 (1990).

[80] A. V. Oppenheim, R. W. Schafer, and J. R. Buck, *Discrete-time-signal Processing* (Prentice-Hall, Upper Saddle River, NJ, 1999).

[81] R. F. Voss and J. Clarke, Flicker $(1/f)$ noise: Equilibrium temperature and resistance fluctuations, Phys. Rev. B **13**, 556 (1976).

[82] P. Dutta and P. M. Horn, Low-frequency fluctuations in solids: $1/f$ noise, Rev. Mod. Phys. **53**, 497 (1981).

[83] F. N. Hooge, $1/f$ noise, Physica B+C **83**, 14 (1976).

[84] P. Bak, C. Tang, and K. Wiesenfeld, Self-Organized Criticality: An Explanation of the $1/f$ Noise, Phys. Rev. Lett. **59**, 381 (1987).

[85] H. Kantz, A robust method to estimate the maximal Lyapunov exponent of a time series, Phys. Lett. A **185**, 77 (1994).

[86] L. Cao, Practical method for determining the minimum embedding dimension of a scalar time series, Physica D **110**, 43 (1997).

[87] J. Theiler, Some comments on the correlation dimension of $1/f\alpha$ noise, Phys. Lett. A **155**, 480 (1991).

[88] A. D. Seymour and D. R. Lorimer, Evidence for chaotic behavior in pulsar spin-down rates, Month. Not. Roy. Astron. Soc. **428**, 983 (2013).

[89] M. Sano and Y. Sawada, Measurement of the Lyapunov Spectrum from a Chaotic Time Series, Phys. Rev. Lett. **55**, 1082 (1985).

[90] E. A. Novikov, Two-particle description of turbulence, Markov property, and intermittency, Phys. Fluids **1**, 326 (1989).

[91] B. B. Mandelbrot, *The Fractal Geometry of Nature* (Freeman, San Francisco, 1982).

[92] A. Provenzale, A. R. Osborne, A. D. Kirwan, and L. Bergamasco, *The Study of Fluid Parcel Trajectories in Large-scale Ocean Flows*, edited by A. R. Osborne (Elsevier, Amsterdam, 1991).

[93] A. Osborne, A. Ro, and A. Provenzale, Finite correlation dimension for stochastic systems with power-law spectra, Physica D **35**, 357 (1989).

[94] J. F. Muzy, E. Bacry, and A. Arneodo, Multifractal formalism for fractal signals: The structure-function approach versus the wavelet-transform modulus-maxima method, Phys. Rev. E **47**, 875 (1993).

[95] M. Ghil, R. Benzi, and G. Parisi (eds.), *Turbulence and Predictability in Geophysical Fluid Dynamics and Climate Dynamics* (North-Holland Publishing, Amsterdam/New York, 1985) p. 449.

[96] R. Benzi, G. Paladin, G. Parisi, and A. Vulpiani, Characterisation of intermittency in chaotic systems, J. Phys. A **18**, 2157 (1985).

[97] B. B. Mandelbrot, Intermittent turbulence in self-similar cascades: Divergence of high moments and dimension of the carrier, J. Fluid Mech. **62**, 331 (1974).

[98] R. Benzi, G. Paladin, G. Parisi, and A. Vulpiani, On the multifractal nature of fully developed turbulence and chaotic systems, J. Phys. A **17**, 3521 (1984).

[99] K.-A. Liu and L. I, Multifractal dynamics of turbulent flows in swimming bacterial suspensions, Phys. Rev. E **86**, 011924 (2012).

[100] F. Schmitt and D. Marsan, Stochastic equations generating continuous multiplicative cascades, Eur. Phy. J. B **20**, 3 (2001).

[101] J. Elder and P. E. Kennedy, More on F versus t tests for unit roots when there is no trend, Econ. Bull. **3**, 1 (2001).

[102] D. A. Dickey and W. A. Fuller, Distribution of the estimators for autoregressive time series with a unit root, J. Am. Stat. Assoc. **74**, 427 (1979).

[103] J. A. Hartigan and M. A. Wong, Algorithm as 136: A k-means clustering algorithm, J. Roy. Stat. Soc **28**, 100 (1979).

[104] G. R. Bowman, V. S. Pande, and Frank Noe, *An Introduction to Markov State Models and Their Application to Long Timescale Molecular Simulation* (Springer Science and Business Media, Berlin, 2013), Vol. 797.

[105] S. Karlin, *A First Course in Stochastic Processes* (Academic Press, New York, NY, 1966).